

1 **Emission and Combustion Characteristics of Ammonia/Methane**
2 **Mixtures for Carbon Reduction and Alternative Fuel Development**

3 Filip Jurić*

4 Faculty of Mechanical Engineering and Naval Architecture
5 University of Zagreb, Zagreb, Croatia
6 e-mail: filip.juric@fsb.unizg.hr

7
8 Marko Ban

9 SDEWES Centre, Zagreb, Croatia
10 e-mail: marko@sdewes.org

11
12 Jakov Baleta*

13 Faculty of Metallurgy, University of Zagreb, Sisak, Croatia
14 e-mail: baleta@simet.unizg.hr

15
16 Stanislav Honus

17 Faculty of Mechanical Engineering, VŠB-Technical University of Ostrava, Ostrava-
18 Poruba, Czech Republic
19 e-mail: stanislav.honus@vsb.cz

20
21 Neven Duić

22 Faculty of Mechanical Engineering and Naval Architecture
23 University of Zagreb, Zagreb, Croatia
24 e-mail: neven.duic@fsb.unizg.hr

25
26 Milan Vujanović*

27 Faculty of Mechanical Engineering and Naval Architecture
28 University of Zagreb, Zagreb, Croatia
29 e-mail: milan.vujanovic@fsb.unizg.hr

30
31
32 **ABSTRACT**

33 The reduction of fossil fuel consumption is of great importance in achieving the targets
34 set forth in the Paris Agreement. One solution to reduce carbon emissions is the utilization of
35 renewable energy sources and alternative fuels, despite the variability that comes with them.
36 Energy storage and vectors are essential in overcoming variability and achieving a faster
37 transition to renewable sources. Ammonia is increasingly being used as an energy vector due
38 to its suitability for transport and utilization in existing combustion systems, even more so than

* Corresponding authors

39 hydrogen. Existing natural gas burners can be modified without extensive adaptations for
40 ammonia/methane mixtures and pure ammonia. To determine combustion parameters and
41 evaluate emission properties, a combination of computational fluid dynamics (CFD) and
42 experimental research is commonly used. This study focuses on generating laminar flame speed
43 and autoignition ammonia/methane mixture databases as input data for combustion CFD
44 modeling, employing LOGE™ software and developed methods with correlation functions.
45 Databases are used as lookup tables for autoignition criteria and laminar flame speed in 3D
46 CFD coherent flame model. Three-zone extended coherent flame model (ECFM-3Z) is used in
47 this study as a CFD combustion model. The generated databases are validated against
48 experimental data from premixed burner and shock tube experiments. A database for
49 autoignition was generated using non-dimensional constant pressure reactors and the San Diego
50 mechanism. The grid for the autoignition database is defined by five parameters: pressure,
51 temperature, equivalence ratio, exhaust gas recirculation, and ammonia/methane ratio. The
52 laminar flame speed database was generated with one-dimensional freely propagating reactors
53 and the same mechanism. Special attention and new developed modelling approach was given
54 to define appropriate correlation methods for unsuccessfully calculated data in unstable
55 regimes. Thus, the first CFD-ready lookup database (345 k auto-ignition points + 18 k
56 laminar-flame-speed points) for NH₃/CH₄ blends is presented, enabling rapid yet accurate
57 decarbonisation studies.

58

59 **KEYWORDS:** Ammonia, Methane, Autoignition, Laminar Flame Speed, Combustion, CFD

60 **1. INTRODUCTION**

61 Reduction of fossil fuel consumption is crucial to achieve the Paris agreement targets.
62 Utilization of renewable energy sources (RES) emerges as a solution for the reduction of carbon
63 emissions, despite the RES variability. Energy storage and vectors are crucial to overcoming
64 variability and achieving a faster transition of renewable sources, with ammonia progressively
65 imposed as an energy vector more suitable for transport and utilization in existing combustion
66 systems than hydrogen. Existing natural gas burners can be modified without extensive
67 adaptations for ammonia/methane mixtures and even for pure ammonia. However, there are
68 drawbacks to its usage, mainly lower heating value, toxicity, and lower laminar flame speeds
69 [1]. Ammonia having a narrow flammability range makes it safer for transport and storage, but
70 it also has a strong influence on the combustion characteristics, which can, for instance, cause
71 slipping in gas turbines and high NO emissions [2]. To counter the above-mentioned drawbacks
72 and successfully use ammonia in gas turbines, engines, and industrial furnaces, various
73 techniques are proposed, including co-firing ammonia with an enhancing species (e.g. methane,
74 hydrogen, or even coal).

75 Utilization of ammonia in existing combustion systems is still impossible without
76 additional burner or injection system modification. That is why, in this work, the authors were
77 mainly focused on ammonia/methane blends applicable in existing combustion systems and
78 where methane flame helps achieve the stable flame regime of ammonia combustion. The
79 ammonia/methane blends are compromise solution in current energy transition, which
80 decreases the burnt methane, but also employs directly in existing natural gas combustion
81 systems.

82 In terms of numerical investigation of ammonia properties and practical use in
83 combustion systems, great importance is put on developing quality chemical mechanisms that
84 can be used in simulations, not only burning pure ammonia but also, as mentioned, in a mixture
85 with other combustible species. The studies developing such mechanisms primarily focused on
86 reducing NO_x emissions, mostly done in premixed flame setups [3]. These mainly fixated on
87 detecting flame intermediates or matching measured values of adiabatic flame speeds.

88 The first comprehensive ammonia oxidation model was developed by Miller et al. [4],
89 consisting of 98 reactions. Based on previous studies, Lindstedt et al. [5] developed a detailed
90 chemical kinetic model consisting of 95 reactions and 21 species. This model was able to
91 reproduce a wider range of temperatures and equivalence ratios. To enable the modelling of
92 ammonia oxidation with present hydrogen, CO, and methane, a detailed mechanism was
93 developed by Skreiberg et al. [5] with a total of 191 reactions. A mechanism consisting of 41
94 species and 250 reactions was proposed by Dagaut et al. [6]. This model put focus on the
95 kinetics of oxidation of hydrogen cyanide (HCN). A larger kinetic mechanism was then
96 proposed by Mével et al. [7], with 203 reactions and 32 species in an effort to describe
97 hydrogen-nitrous oxide delay times at high pressures. Coda Zabetta and Hupa [8] published a
98 mechanism intended for biomass combustion chemistry composed of 371 reactions and 60
99 species, but this mechanism could also be applied to ammonia oxidation and its blends with
100 methane, while Klippenstein et al. [9] focused on the thermochemistry and reactions of NNH
101 in NO formation. As mentioned earlier, premixed flames were the focus of various research,
102 and Tian et al. [10] studied 11 premixed NH₃/CH₄/O₂/Ar flames and finally, based on the
103 research results, created and updated chemical mechanism consisting of 84 species and 703
104 elementary reactions. Finally, Mendiara and Glarborg [11] also updated an existing mechanism
105 in order to improve the description of the effect of high CO₂ concentration on ammonia
106 chemistry during methane oxidation ending up with the mechanism consisting of 97 species
107 and 779 elementary reactions.

108 Recent studies further emphasize ammonia/methane blends as a feasible pathway for
109 reducing emissions and stabilizing ammonia flames. Liu et al. [12] examined ammonia as a
110 marine fuel, identifying liquid ammonia's advantages in efficiency and NO_x control. Jójka et al.
111 [13] investigated swirl flames, finding that, although internal recirculation zones stabilize
112 ammonia/methane flames, they also concentrate NO formation. Wei et al. [14] demonstrated
113 hydrogen's potential to improve flame speed and stability in ammonia blends, thereby reducing
114 extinction risks. Numerical and experimental works, such as those by Zhang et al. [15] and
115 Guiberti et al. [16], demonstrate swirl intensity's role in controlling NO emissions and the
116 viability of ammonia for carbon-neutral power systems. Okafor et al. [17] proved utility of
117 reduced-order models for simulating methane-ammonia combustion under gas turbine
118 conditions, achieving a balance between computational efficiency and accuracy. Very recent
119 studies have reiterated the need for fast-running but chemistry-rich CFD tools [13].

120 Detailed chemical mechanisms exist for NH₃ oxidation, but embedding these large
121 kinetics (tens of species, hundreds of reactions) directly into 3D CFD simulations is
122 prohibitively expensive. An effective solution is to precompute key combustion parameters –
123 such as laminar flame speeds and autoignition delay times – over a range of conditions and
124 store them in a look-up table that the CFD solver can query during runtime. By generating
125 tabulated chemistry that collapses 300+ species to two scalar look-up tables, we address

126 precisely this need. A comprehensive database of laminar flame speeds and autoignition delay
127 times for NH₃/CH₄ mixtures across a wide range of pressures, temperatures, equivalence ratios,
128 and fuel blend fractions is presented. This CFD-ready database using the capabilities of San
129 Diego mechanism [18] that features 68 chemical species and 311 chemical reactions is
130 integrated into a three-zone Extended Coherent Flame Model (ECFM-3Z) as look-up tables,
131 enabling efficient simulations of ammonia/methane combustion. A novel correlation method is
132 introduced to handle conditions where direct kinetic calculations fail (unstable combustion
133 regimes), filling in missing data and ensuring a complete dataset. This approach enables the
134 efficient simulation of complex combustion dynamics under varied operating conditions. The
135 pre-generated databases enable accurate predictions of combustion characteristics, such as
136 flame stability, pollutant formation, and thermal performance, facilitating the integration of
137 ammonia/methane blends into industrial systems. To the authors' knowledge no public
138 high-resolution chemistry database exists for CFD combustion of NH₃/CH₄, so this study fills
139 that gap. The accuracy of the tabulated results is confirmed by comparison with experimental
140 flame speed and ignition delay measurements, whilst the CFD simulation is run on the case of
141 experimental premixed swirl burner for which there are available measured data.

142 2. METHODOLOGY

143 For chemistry calculation, LOGEsoft™ software was used. The first section will
144 describe the methodology for the generation of an autoignition timing database, followed by
145 the laminar flame speed procedure.

146 2.1. Autoignition methodology

147 The chemistry solver calculations of 0D constant pressure reactors were defined with the
148 four-dimensional grid, where the parameters were temperature, pressure, equivalence ratio (φ),
149 and fuel fraction of CH₄ in NH₃/CH₄ mixture. The calculations were performed on perfectly
150 stirred reactors, where each combination of the four previously mentioned parameters was
151 calculated as a separate reactor.

152 The method for calculating the main ignition delay time and cool flame delay time is
153 based on a robust procedure that is regardless of the mechanism and type of fuel [19]. It
154 observes the temperature profile in time, stores its inflexion points, and is shown in Figure 1.
155 After the inflexion points are obtained, the time at the first inflexion point is set as cool flame
156 delay time, and the last inflexion point, before the achieved equilibrium state, is set as the main
157 ignition delay time. The second inflexion point (between the first and the last inflexion point)
158 is selected as the end timing (reset point) of specific cool flame heat release. Until that timing
159 (reset point), the specific cool flame heat release is obtained from the integrated heat release
160 curve in time (calculated from enthalpy curves).

161

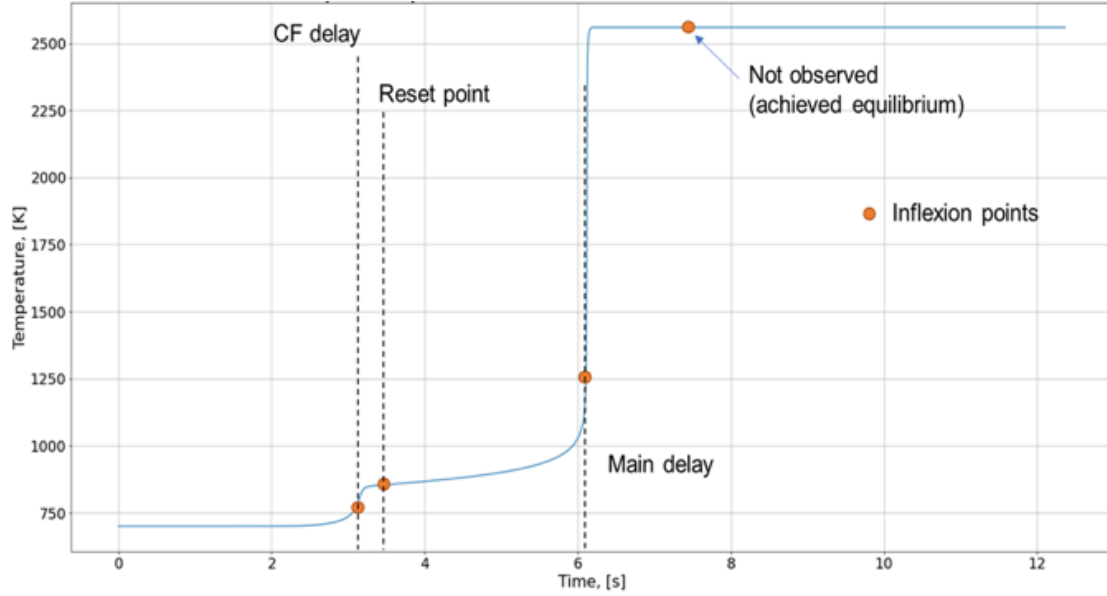


Figure 1 Autoignition calculation method

The raw calculated data were sorted in the eight-dimensional matrix, where the four additional output parameters were autoignition timing, cold flame autoignition timing, released heat, and heat released by cold flame. For the filling of the unsuccessfully calculated autoignition timing points, AIG , correlation function from [20] was applied in pressure and equivalence ratio directions:

$$AIG(p, \varphi, Y_f) = AIG_{ref} \left(\frac{p}{p_{ref}} \right)^\alpha (\varphi)^\beta \quad (1)$$

where α and β are two tuning parameters that were calculated for each combination of the temperature and fuel fraction. For the calculation of α and β parameters that have the lowest disagreement with the raw calculated data, the nonlinear least-squares method was employed with the Levenberg-Marquardt algorithm. Additionally, the algorithm was set to bisquare robust regression. The algorithm is based on SciPy open-source package and its function `scipy.optimize.least_squares`. The objective function is defined as

$$F_{AIG} = \min \sum_{i=1}^{N_{p,\varphi}} [AIG_i - AIG(p_i, \varphi_i)]^2 \quad (2)$$

where the objective function is approximated by the linearization in each iteration step. The φ is changed with the estimation $\varphi + \delta$, and to determine δ the following term has to be calculated:

$$F_{AIG} \approx AIG(p_i, \varphi_i + \delta) + \frac{\partial AIG(p_i, \varphi_i)}{\partial \varphi} \delta \quad (3)$$

As in the case of the laminar flame speed algorithm was set to bisquare robust regression.

183 2.2.Laminar Flame Speed methodology

184 The raw calculated data from 1D flame reactors were sorted in the four-dimensional
 185 matrix. The chemistry solver calculations were defined with the four-dimensional grid, the
 186 same as in autoignition procedure. The calculations were performed on premixed freely
 187 propagating reactors, where each combination of four parameters was calculated as a separate
 188 reactor. The raw calculated data were sorted in the five-dimensional matrix, where the fifth
 189 dimension is calculated as laminar flame speed.

190 Unsuccessfully calculated data were imputed with the correlation function for laminar
 191 flame speed defined as the log-normal distribution for equivalence ratio and as the exponential
 192 function for the pressure direction. The tuning equation has the following form [20]:
 193

$$S_L(p, \varphi) = S_{L, ref} \left[\frac{1}{\varphi \sigma \sqrt{2\pi}} \exp\left(-\frac{(\ln \varphi - \mu)^2}{2\sigma^2}\right) \right] \left(\frac{p}{p_{ref}}\right)^\beta \quad (4)$$

194 where μ and σ are two tuning parameters that are calculated for each combination of the
 195 temperature and EGR. For the calculation of μ and σ parameters that have the lowest
 196 disagreement with the raw computed data, the nonlinear least-squares method was employed
 197 with the Levenberg-Marquardt algorithm and bisquare robust regression.
 198

199 2.3.Computational Fluid Dynamics

200 Combustion model ECFM-3Z is based on an equation for flame surface density that
 201 incorporates the impact of turbulent eddies on the wrinkling of the flame front surface. In the
 202 ECFM-3Z model, all computational cells are split into three regions to describe non-premixed
 203 combustion: unmixed fuel zone, mixed zone, and unmixed initial air zone [21]. The overall
 204 state influences each zone within the computational cell. If the fuel is introduced into the system
 205 and observed in a representative computational cell, initially only consisting of unburned and
 206 unmixed air, the fuel occupies a finite amount of cell space after evaporation. During this stage,
 207 it remains unmixed with the existing air, thereby creating two zones (unmixed and unburned
 208 air and unmixed and unburned fuel). Subsequently, the fuel and air begin to mix within the
 209 intermediate zone, giving rise to the third zone, which is mixed and unburned. At this point, the
 210 mixed zone is prepared for monitoring the ignition criterion. Once the ignition criterion is met,
 211 combustion initiates and propagates through the mixed zone, dividing it into two sub-zones: the
 212 burnt and unburned mixed zone. The representation of gas state determines the fundamental
 213 transport equations in the ECFM-3Z model through two properties: progress variable c and the
 214 mixture fraction Z . Additionally, transport equations for the following species are also solved
 215 [20]: oxygen (O_2), nitrogen (N_2), nitrogen monoxide (NO), CO_2 , carbon monoxide (CO),
 216 hydrogen (H_2), H_2O , hydrogen (H) and nitrogen (N) cation, oxygen (O), hydroxide (OH)
 217 anions.
 218

$$\frac{\partial \bar{\rho} \tilde{Y}_X}{\partial t} + \frac{\partial \bar{\rho} \tilde{u}_i \tilde{Y}_X}{\partial x_i} = \frac{\partial}{\partial x_i} \left(\left(\frac{\mu}{Sc} + \frac{\mu_t}{Sc_t} \right) \frac{\partial \tilde{Y}_X}{\partial x_i} \right) + \bar{\rho} \tilde{S}_X \quad (5)$$

219 t is the time variable, x_i is the space coordinate, μ is dynamic viscosity. Sc is Schmidt number,
 220 and t index indicates turbulent values. The turbulent Schmidt number is defined similarly,
 221 incorporating both the turbulent momentum transfer (eddy viscosity) and the turbulent mass
 222 transfer. \tilde{S}_X is the mass-specified source term of chemical species X and \tilde{Y}_X is its average mass
 223 fraction, which is defined as:

$$\tilde{Y}_X = \frac{\overline{m_x}}{\overline{m}} \quad (6)$$

224 where $\overline{m_x}$ is the average mass of species X , and \overline{m} is the total mass inside a cell. The previously
 225 defined general transport equation is divided to account for the burned and unburned subzones
 226 of the computational cell when considering the fuel species.

$$\frac{\partial \rho \tilde{Y}_{uF}}{\partial t} + \frac{\partial \rho \tilde{u}_i \tilde{Y}_{uF}}{\partial x_i} = \frac{\partial}{\partial x_i} \left(\left(\frac{\mu}{Sc} + \frac{\mu_t}{Sc_t} \right) \frac{\partial \tilde{Y}_{uF}}{\partial x_i} \right) + \rho \tilde{S}_F c + \overline{\dot{\omega}_{uF}} - \overline{\dot{\omega}_{u \rightarrow b}} \quad (7)$$

$$\begin{aligned} \frac{\partial \rho \tilde{Y}_{bF}}{\partial t} + \frac{\partial \rho \tilde{u}_i \tilde{Y}_{bF}}{\partial x_i} \\ = \frac{\partial}{\partial x_i} \left(\left(\frac{\mu}{Sc} + \frac{\mu_t}{Sc_t} \right) \frac{\partial \tilde{Y}_{bF}}{\partial x_i} \right) + \rho \tilde{S}_F (1 - c) + \overline{\dot{\omega}_{bF}} + \overline{\dot{\omega}_{u \rightarrow b}} \end{aligned} \quad (8)$$

227 This partition of the fuel species into the unburned \tilde{Y}_{uF} , and burned \tilde{Y}_{bF} is necessary to enable
 228 the influence of both propagating and diffusion flames. The rate of gaseous fuel production,
 229 resulting from phenomena such as the evaporation of liquid fuel droplets, is represented by the
 230 symbol \tilde{S}_F . This production rate is distributed between the burned and unburned sub-zones
 231 based on the progress variable \tilde{c} . The progress variable is calculated based on the assumption
 232 that the flame is an interface of infinitesimal thickness that separates the fresh gases from the
 233 burned gases and is given in Equation (9), where $\overline{\tilde{Y}_{TuF}}$ is the fuel mass fraction before the start
 234 of the combustion.

$$c = 1 - \frac{\overline{\tilde{Y}_{uF}}}{\overline{\tilde{Y}_{TuF}}} \quad (9)$$

235 The reaction rate at which the unburned fuel is consumed in propagating flame is represented
 236 by the variable $\overline{\dot{\omega}_{uF}}$, and the rate on the opposite side represents the burned fuel oxidation in
 237 diffusive flame. The rates of fuel consumption are influenced by the local flame surface density
 238 and laminar flame velocity, and their calculations are outlined in the following section. In
 239 situations where the local equivalence ratio is rich, the unburned sub-zone lacks sufficient
 240 oxygen to completely consume all the unburned fuel. As a result, a portion of the unburned fuel
 241 represented with the term $\overline{\dot{\omega}_{u \rightarrow b}}$ is transferred into the burned sub-zone through the source term.
 242 $\overline{\dot{\omega}_{u \rightarrow b}}$ is the source term due to the mixing process, which is defined as the turbulent properties
 243 and partial fuel density.

$$\overline{\dot{\omega}_{u \rightarrow b}} = \frac{\varepsilon}{k} \frac{\tilde{Y}_{Fu}}{\rho_{Fu}} (1 - \tilde{Y}_{Fu}) \quad (10)$$

244 where k is turbulent kinetic energy and ε is the rate of turbulent energy dissipation from the
 245 turbulence model. Through the mixing turbulent time scale, turbulence interacts with the
 246 development of the combustion process.

247 In ECFM-3Z, the fuel combustion rate per unit volume is defined as the product of flame
 248 surface density and the local fluid velocity of the fuel/oxidizer mixture. The transport equation
 249 of flame surface density, Σ is defined as [21]:

250

$$\frac{\partial \Sigma}{\partial t} + \frac{\partial \tilde{u}_i \Sigma}{\partial x_i} = \frac{\partial}{\partial x_i} \left(\frac{1}{\bar{\rho}} \left(\frac{\mu}{S_c} + \frac{\mu_t}{S_{c_t}} \right) \frac{\partial \Sigma}{\partial x_i} \right) + (P_1 + P_2 + P_3) \Sigma - D \quad (11)$$

251 In the above equation, besides already defined convection, diffusion and unsteady terms, on
 252 the right side of the equation, the following source terms are introduced.

$$P_1 = 1.6 K_t \quad (12)$$

253 This property is flame surface production by turbulent stretch being net flame stretched, K_t .
 254 The second of the sink terms represents the flame surface production by mean flow dilatation
 255 and is modelled as:

$$P_2 = \frac{2}{3} \frac{\partial \tilde{u}_i}{\partial x_i} \quad (13)$$

256 The last term in the section appearing next to the flame surface density, P_3 describes the effects
 257 of the flame expansion and curvature in the following manner:

$$P_3 = \frac{2}{3} S_L \frac{1-c}{c} \Sigma \quad (14)$$

258 The sink term in the equation is the destruction term due to fresh gas consumption defined by
 259 the equation:

$$D = S_L \frac{\Sigma^2}{1-c} \quad (15)$$

260 where \tilde{S}_{mix} is the source term due to the mixing process, which is defined as the turbulent
 261 properties and partial fuel density.

$$\tilde{S}_{mix} = -\frac{\varepsilon_t \tilde{Y}_{Fu}}{k_t \rho_{Fu}} (1 - \tilde{Y}_{Fu}) \quad (16)$$

262 where k is turbulent kinetic energy, and ε is the rate of turbulent energy dissipation from the
 263 turbulence model. Through the mixing turbulent time scale, turbulence interacts with the
 264 development of the combustion process.

$$\overline{\dot{\omega}_{uF}} = \bar{\rho} \tilde{Y}_{uF} \Sigma S_L \quad (17)$$

265 Within the ECFM-3Z combustion model, a straightforward methodology for ignition tracking
 266 is employed, drawing inspiration from the approach commonly utilized for predicting knocking
 267 in gasoline engines. This involves introducing a tracking intermediate species, denoted as I,
 268 which is entirely hypothetical and solely serves to determine the initiation time of ignition
 269 accurately. Initially, it was utilized exclusively to track the primary ignition. However, as
 270 suggested from literature, this principle can also be extended to account for low-temperature

271 ignition, thereby incorporating the simulation of cool flame phenomena. In the combustion
 272 model, the intermediate species undergo temporal evolution based on the following equation:

$$\frac{\partial \bar{\rho} \tilde{Y}_I}{\partial t} = \tilde{Y}_F \frac{\sqrt{\tau_d^2 + 4(1 - \tau_d) \frac{\tilde{Y}_I}{\tilde{Y}_F}}}{\tau_d} \quad (18)$$

273

274 2.3.1. NOx modelling in ECFM-3Z

275 In general, the most significant NO source in burner is thermal NO. One of the most
 276 widely used NO models in combination with combustion models is the extended Zeldovich
 277 mechanism:



278 where k_1 , k_2 , k_3 are forward and backward reaction rates. For the extended Zeldovich
 279 mechanism, the additional impact of O₂ and N₂ in the presence of hydrogen radicals is
 280 considered. It is worth noting that all three reactions exhibit a strong temperature dependency,
 281 where the change of NO concentration over time is given by:

282

$$\begin{aligned} \frac{dc_{\text{NO}}}{dt} = & k_{1f}c_{\text{O}}c_{\text{N}_2} + k_{2f}c_{\text{N}}c_{\text{O}_2} + k_{3f}c_{\text{N}}c_{\text{OH}} - k_{1b}c_{\text{NO}}c_{\text{N}} - k_{2b}c_{\text{NO}}c_{\text{O}} \\ & - k_{3b}c_{\text{NO}}c_{\text{H}} \end{aligned} \quad (22)$$

283 where c denotes the concentration of indexed chemical species, while b and f denote backward
 284 and forward reactions.

285 3. NUMERICAL SETUP

286 Experimental data was gathered from a premixed swirl burner characterized by a
 287 geometric swirl number of 1.05, as shown in Error! Reference source not found.. This burner
 288 is a component of the experimental setup located at Cardiff University's Gas Turbine Research
 289 Centre. Within the combustion chamber, a premixed combination of ammonia, methane, and
 290 air is introduced through a swirler, contained within a quartz tube that confines the flame.
 291 Concentrations of NO, CO₂, CO, and O₂ were measured at the exit of the quartz tube, with a
 292 measurement error of approximately 5%. To conduct a grid dependency study, three structured
 293 computational meshes were generated, offering different resolutions: 70,922 (coarse), 155,436
 294 (medium), and 321,328 (fine) volumes. The reference indicated that the coarse mesh was
 295 largely sufficient for most results, striking a favorable balance between accuracy and
 296 computational demand.

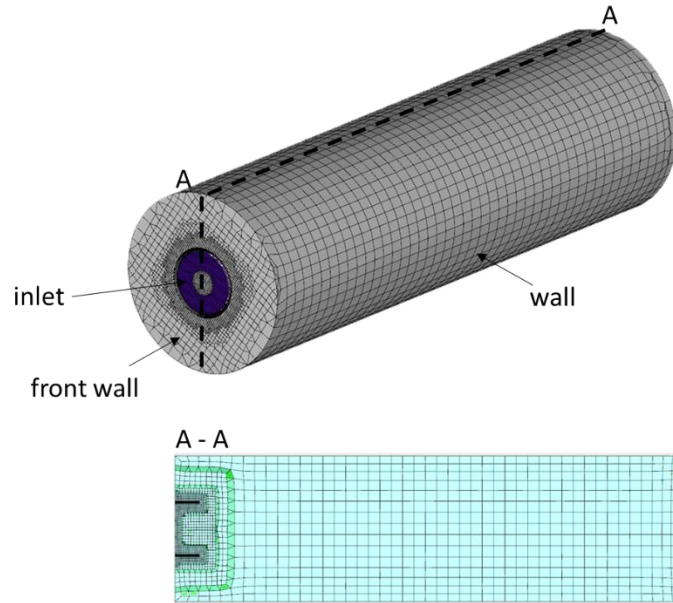


Figure 2 Computational mesh

297
298
299
300
301
302
303
304
305
306
307

Table 1 presents simulated scenarios from the current study, where equivalence ratios ranged from 0.81 to 1.24, maintaining a constant burner power of 44 kW. Notably, the flow rates of ammonia and methane remained constant while the equivalence ratio was altered by adjusting the oxidizing air, which are also stated in Table 1. For a comprehensive understanding of the experimental setup, interested individuals are encouraged to refer to for further details [22]. Methane gas flow was 0.47 g/s.

Table 1 Operating points and inlet specifications

Equivalence ratio, -	Air mass flow, g/s	Ammonia mass flow, g/s
0.81	16.66	0.8
1.02	13.25	0.82
1.14	11.88	0.82
1.24	10.86	0.82

308
309
310
311
312
313
314
315
316
317
318
319
320

Employing a cylindrical form, the computational domain encompasses only the combustion space, as depicted in Figure 2. A time step size of 0.5 milliseconds was chosen because it consistently achieved a convergent solution within 100 iterations at each time step, eliminating the need for additional sensitivity analysis. The momentum and continuity equations utilized a central differencing scheme, while a simple upwind differencing scheme was applied to the turbulence and energy equations.

The equivalence ratio, which compares the operational fuel/air ratio to the stoichiometric fuel/air ratio, dictates the combustion state. Stoichiometric combustion occurs at a ratio of one, while ratios less than one indicate fuel-lean conditions and ratios greater than one signify fuel-rich conditions. Inlet velocities of 24.1, 19.88, 18.11, and 16.71 ms^{-1} for the air/ammonia/methane mixture corresponded to equivalence ratios of 0.8, 1.02, 1.14, and 1.24 at an inlet temperature of 293 K. The wall temperature was set at a constant of 1,500 K [2], and

321 a constant pressure boundary condition of 1 bar was imposed at the outlet. Convergence of the
 322 solution was established when residuals in the transport equations decreased by four orders of
 323 magnitude.

324 In Table 2 and Table 3 are given grid points for which autoignition and laminar flame
 325 speed databases are calculated. The autoignition database resulted in the total number of
 326 345,015 points and laminar flame speed in 18,000 points.

327
 328

Table 2 Autoignition points in database

AIG	Temperature, K			Pressure, bar			EQR, -			EGR (Y_{EGR}), -			Fuel Fraction (Y_F), -			
	MIN	MAX	STEP	MIN	MAX	STEP	MIN	MAX	STEP	MIN	MAX	STEP	MIN	MAX	STEP	
			41			11			17			9			5	
	600	1500		1	250		0.1	6		0	0.8	0.1	0	1	0.2	
	600	1200	25	1	5	4	0.1	0.2	0.1	0	0.8	0.1				
	1200	2000	50	5	10	5	0.2	0.8	0.2							
				10	50	10	0.8	1.2	0.1							
				50	250	50	1.2	2	0.2							
							2	6	1							
														Total number of points:		345015

329
 330
 331

Table 3 Laminar flame speed points in database

SL	Temperature, K			Pressure, bar			EQR, -			EGR (Y_{EGR}), -			Fuel Fraction (Y_F), -			
	MIN	MAX	STEP	MIN	MAX	STEP	MIN	MAX	STEP	MIN	MAX	STEP	MIN	MAX	STEP	
			6			10			15			4			5	
	300	1250		1	300		0.2	5		0	0.6	0.2	0	1	0.2	
	300	500	200	1	5	4	0.2	0.8	0.2							
	500	750	250	5	10	5	0.8	1.2	0.1							
	750	900	150	10	20	10	1.2	2	0.2							
	900	1250	350	20	50	30	2	5	1							
	1250	1500	250	50	300	50										
														Total number of points:		18000

332
 333
 334
 335
 336
 337

For the CFD simulation AVL FireTM software was used. The calculation of the continuity equation employed the central differencing scheme along with the AMG linear solver. For the momentum's convective terms, discretization was achieved using the MINMOD scheme, whereas the turbulence within the energy and combustion transport equations utilized an

338 upwind scheme. Throughout this work, the convergence criterion for all variables was
339 determined by the normalized sum of absolute residual values, set at 10^{-5} .

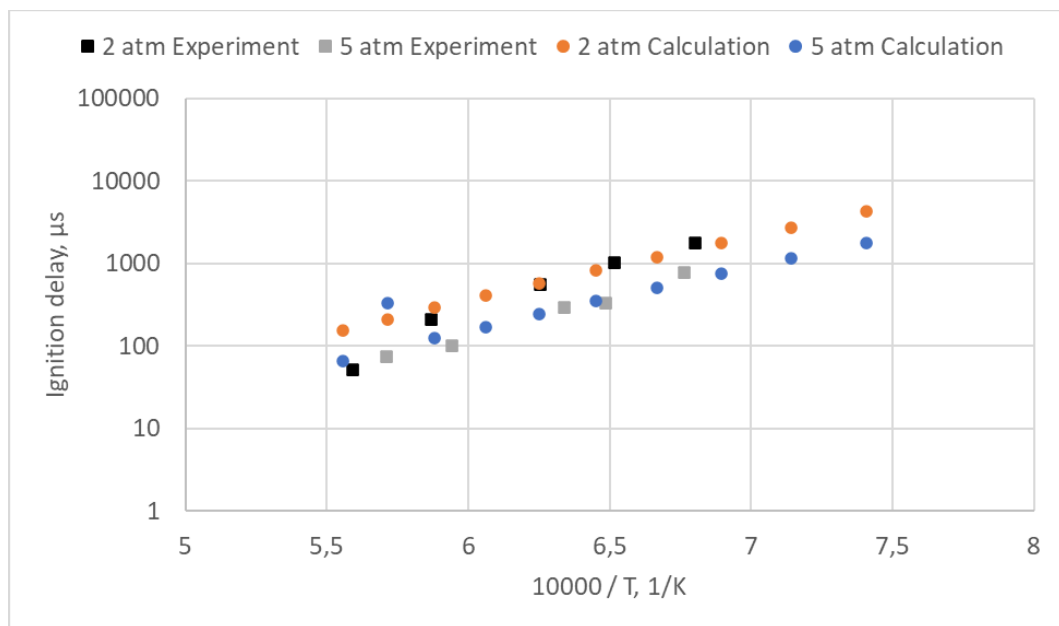
340 4. RESULTS

341 In this section, autoignition timing results with San Diego mechanism are validated
342 against available experimental data for NH_3/CH_4 mixture [23], followed by laminar flame speed
343 validation against the experimental data from [24]. Finally, CFD results are presented.

344 4.1. Autoignition Results

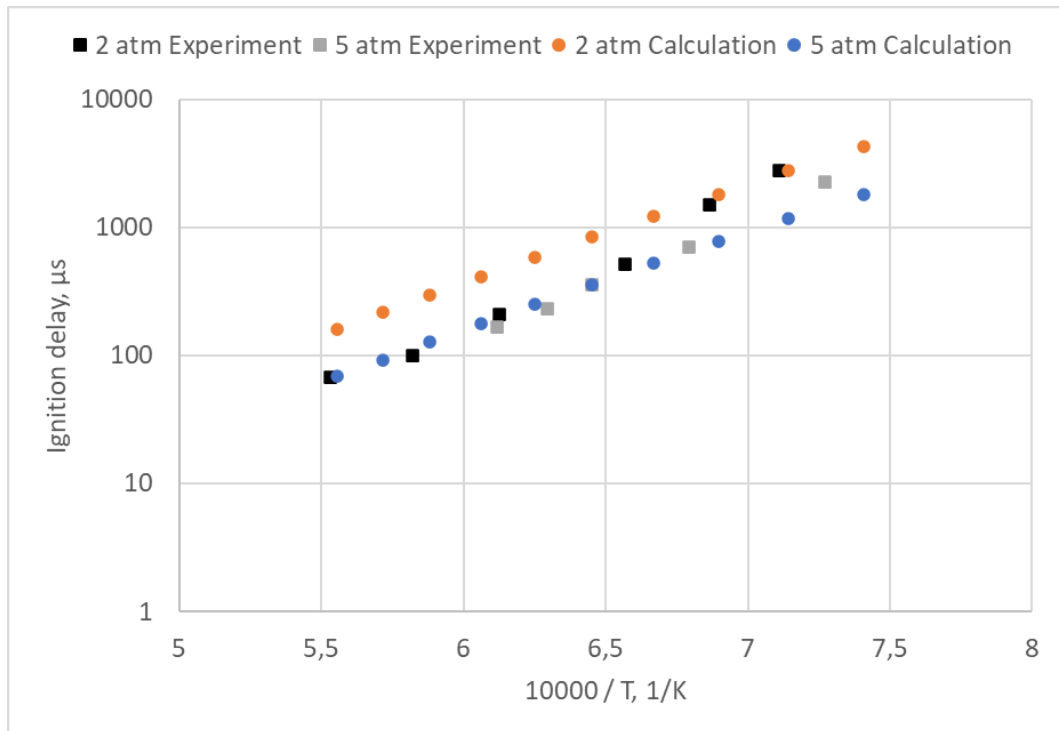
345 In Figure 3–5, the calculated results are validated against experimental results of the
346 ignition delay times for 60% NH_3 / 40% CH_4 fuel blend under the initial pressure conditions of
347 2 and 5 atm, initial temperature between 1369 and 1804 K, and equivalence ratios of 0.5, 1 and
348 2. The agreement between experimental data and results is better for 5 atm and lower
349 temperatures throughout the air/fuel ratios. The highest discrepancy is achieved for higher
350 temperatures, where due to the cold flame ignition, some points have increased calculated
351 observed hot flame autoignition timing. The agreement with the experimental data is achieved
352 in order of magnitude for all three equivalence ratio values.

353

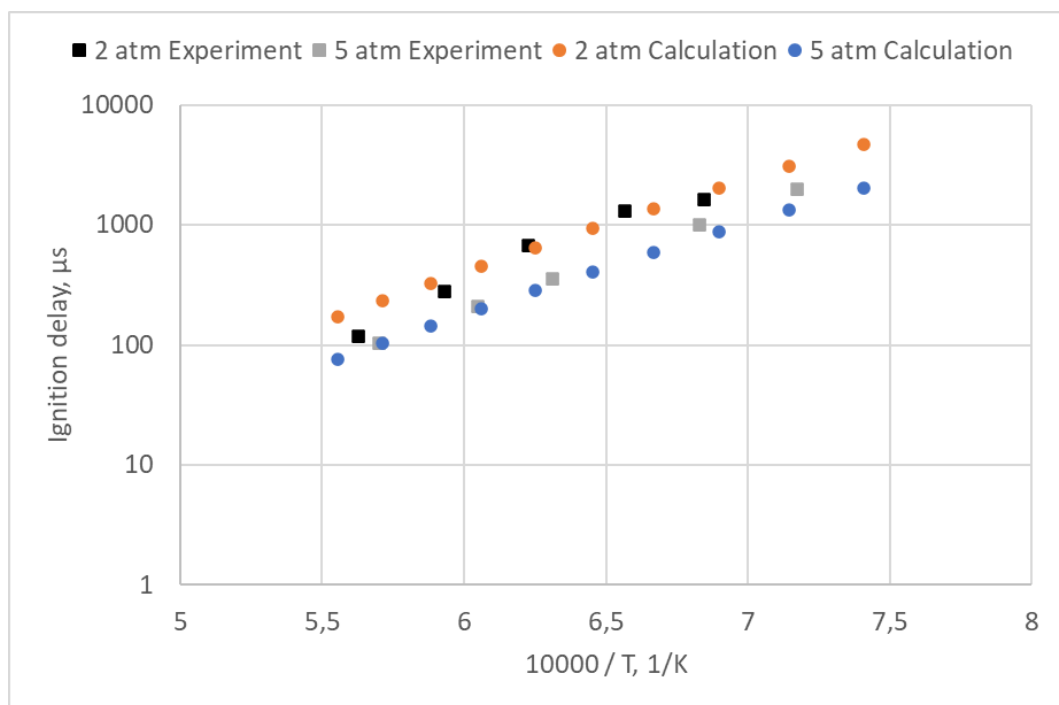


354

355 Figure 3 Comparison of calculated autoignition timing data with experimental data at
356 pressure values 2 atm and 5 atm for equivalence ratio 0.5
357



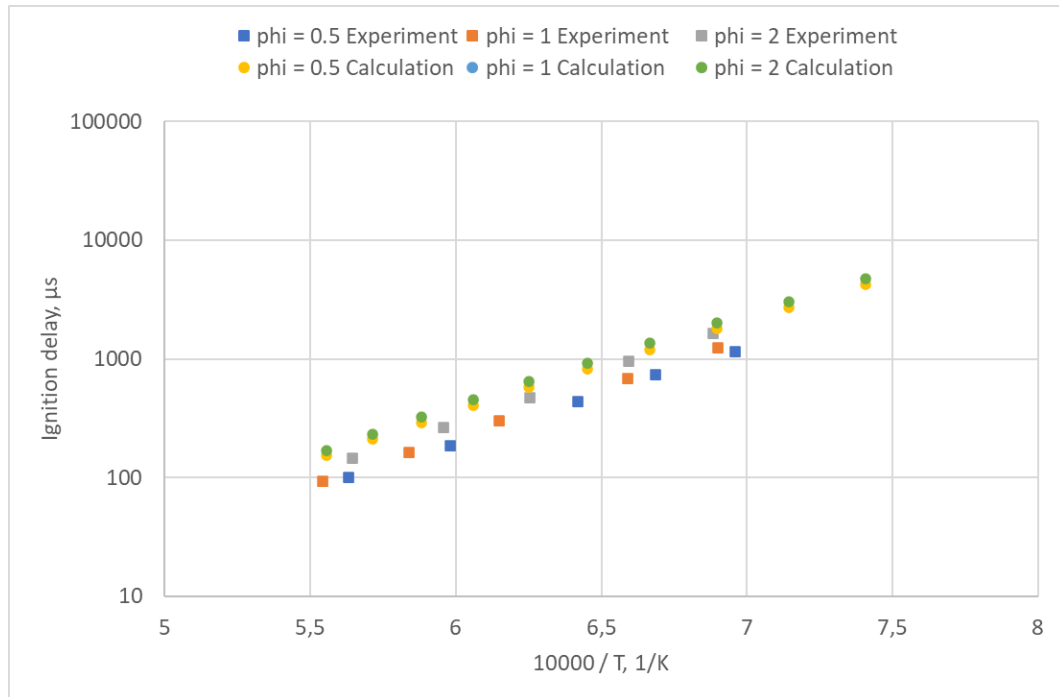
358
359
360
361
362
Figure 4 Comparison of calculated autoignition timing data with experimental data at pressure values 2 atm and 5 atm for equivalence ratio 1



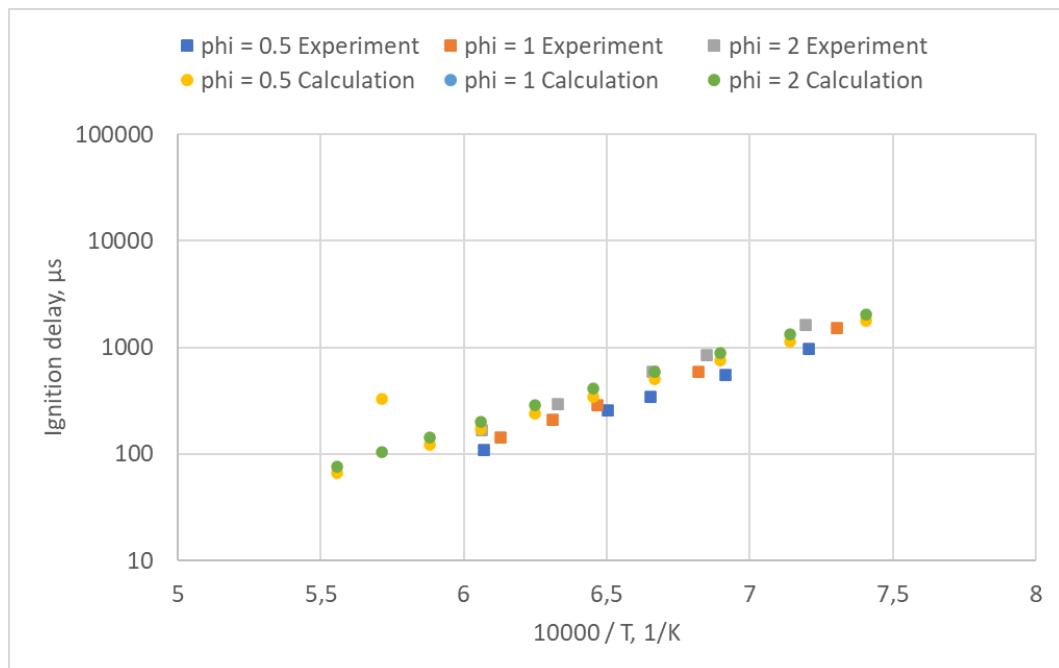
363
364
365
366
367
368
369
Figure 5 Comparison of calculated autoignition timing data with experimental data at pressure values 2 atm and 5 atm for equivalence ratio 2

Figure 6 shows the autoignition timing validation against experimental data at pressure value 2 atm, while Figure 7 shows validation at 5 atm. From the obtained results, it can be observed that the influence of the equivalence ratio is more pronounced in experimental data

370 compared to calculated data, where the results for equivalence ratio one cannot be seen from
 371 the plotted points for equivalence ratio 0.5 and 2. In Figure 7, the discrepancy at high
 372 temperatures is attributed to the autoignition detection algorithm that has detected a cold flame
 373 ignition. The closer agreement at 5 atm relative to 2 atm is attributed to faster chain-branching
 374 ($\text{NH}_2 + \text{O}_2$) at higher pressure, making the mechanism less sensitive to missing secondary
 375 reactions.
 376



377
 378 Figure 6 Comparison of calculated autoignition data with experimental data for
 379 equivalence ratio 0.5, 1.0 and 2.0 at 2 atm
 380



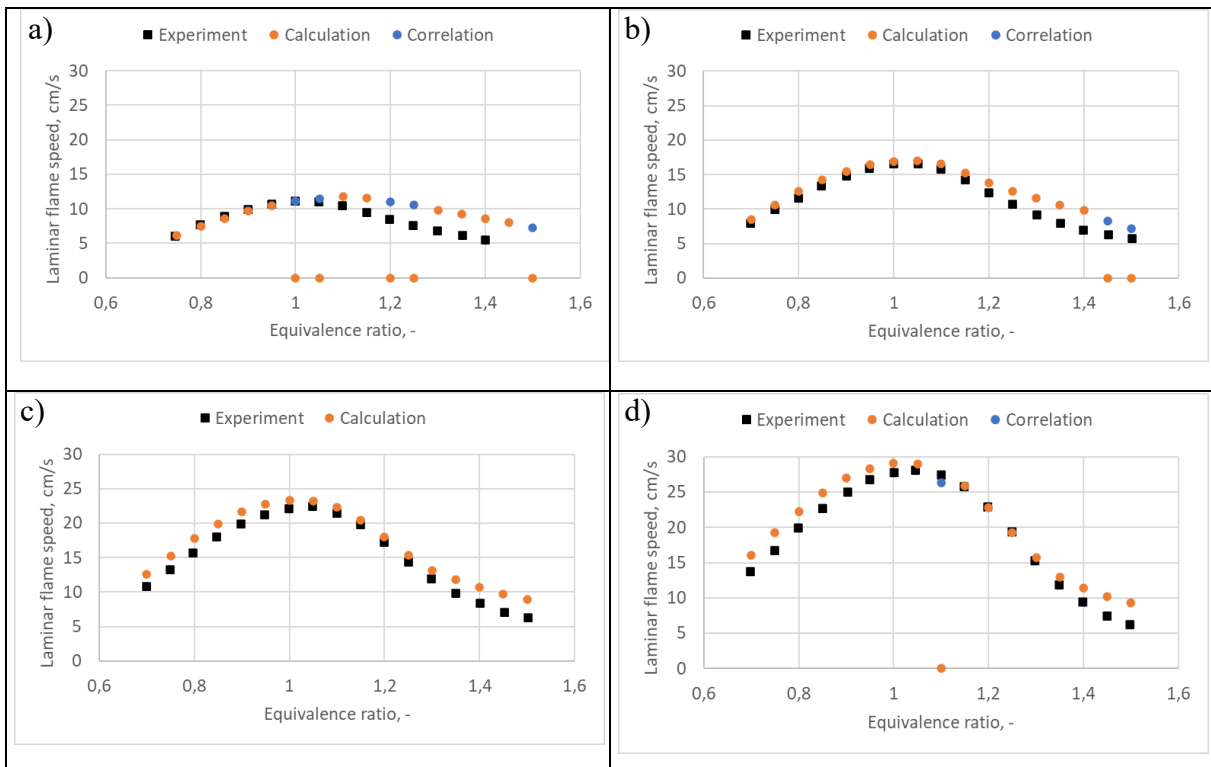
381

382 Figure 7 Comparison of calculated autoignition data with experimental data for
 383 equivalence ratio 0.5, 1.0 and 2.0 at 5 atm
 384

385 **4.2.Laminar Flame Speed Results**

386 All experimental data for laminar flame speed are performed at atmospheric pressure, and
 387 298 K. Figure 8 depicts the calculated data of laminar flame speed at different NH₃/CH₄ blend
 388 ratio with orange dots against the black rectangular that represent the experimental data. The
 389 orange dots are shown at the abscissa for the unsuccessfully calculated data. Additionally, for
 390 unsuccessfully calculated data, results with correlation functions from Equation (1) are shown
 391 with blue dots.

392 The agreement between the calculated data and obtained results is better for the lean
 393 mixtures and around the stoichiometric equivalence ratio. At the same time, a more significant
 394 discrepancy was achieved for the fuel-rich region, which is especially visible in a mixture with
 395 20% mol CH₄ or the highest NH₃ content. That can be attributed to decreased accuracy in the
 396 fuel-rich region of incorporated NH₃ chemical reactions in the San Diego mechanism. A similar
 397 effect is visible in lean mixtures for CH₄, which showed a more significant difference with the
 398 experimental data than NH₃ chemical reactions. For fuel-rich flames the mechanism
 399 over-predicts the measured laminar burning. This is attributable to the missing NNH and NCN
 400 prompt-NO networks, and generic third-body efficiencies for NH₃, all of which become
 401 dominant once the hydrogen-radical pool is depleted. Similar discrepancies have been reported
 402 by Okafor et al. [25] and Rocha et al. [26]. Future work will therefore migrate to the more
 403 accurate mechanism, but this drawback is not critical for the demonstration of suitability of the
 404 method.
 405



406 Figure 8 Validation of calculated laminar flame speed and correlation function results for
407 the unsuccessfully calculated points, NH₃/CH₄ mixture with; a) 20%mol CH₄, b) 40%mol CH₄,
408 c) 60%mol CH₄, d) 80%mol CH₄

409

410 Additionally, in Figure 9, the example of correlation function postprocessing of the raw
411 calculated data is given. The upper figures show the raw data from premixed freely propagating
412 flame reactor, and at the bottom are given results for the same database points after applying
413 the correlation function in Equation (4). At 1500°C, the solver for the 1-D freely premixed
414 propagating flame model exhibited instability, leading to divergence in the flame speed
415 calculations for $\Phi > 3$. These divergent values are represented by zero flame speed. The post-
416 processing procedure employed for the raw data, as outlined in Equation (4), shows values that
417 are influenced by the converged data at $p=5$ bar and $\Phi=3$, explaining the observed trend in the
418 calculated flame speed. It can be acknowledged that the differences between peak laminar flame
419 speeds at stoichiometric and fuel-rich mixtures are less noticeable at lower temperatures.
420 However, given the high temperature (1500°C) and the absence of experimental data at this
421 temperature, the results presented are based on numerical simulations, which may exhibit
422 divergence under extreme conditions. With this approach, the authors focused on a procedure
423 that is robust at high temperatures and will provide meaningful predictions of laminar flame
424 speeds at high temperatures and EGR values.

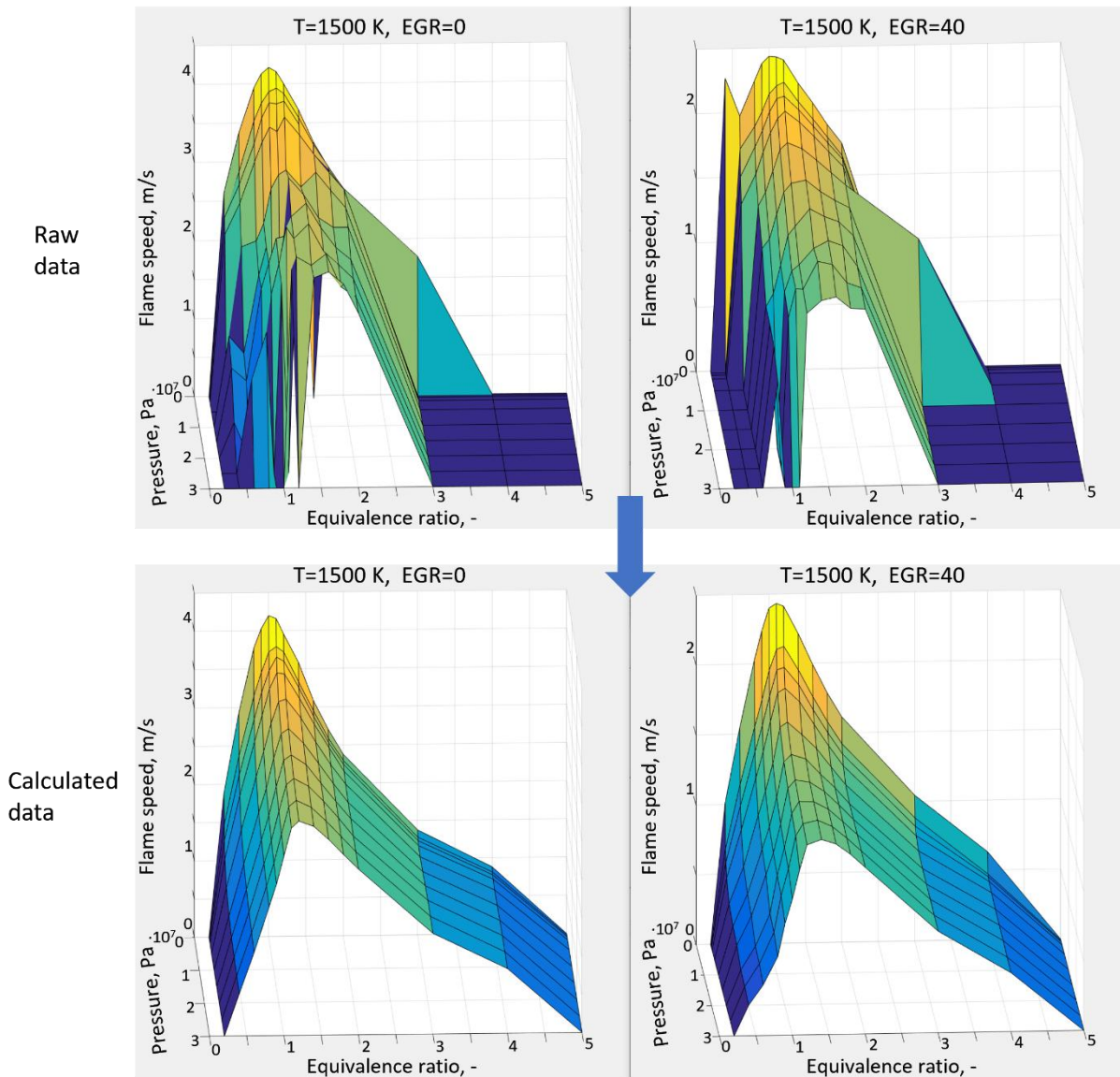


Figure 9 Example of the raw database postprocessing with correlation function: pure ammonia at 1500 K and EGR values: 0%, 40%

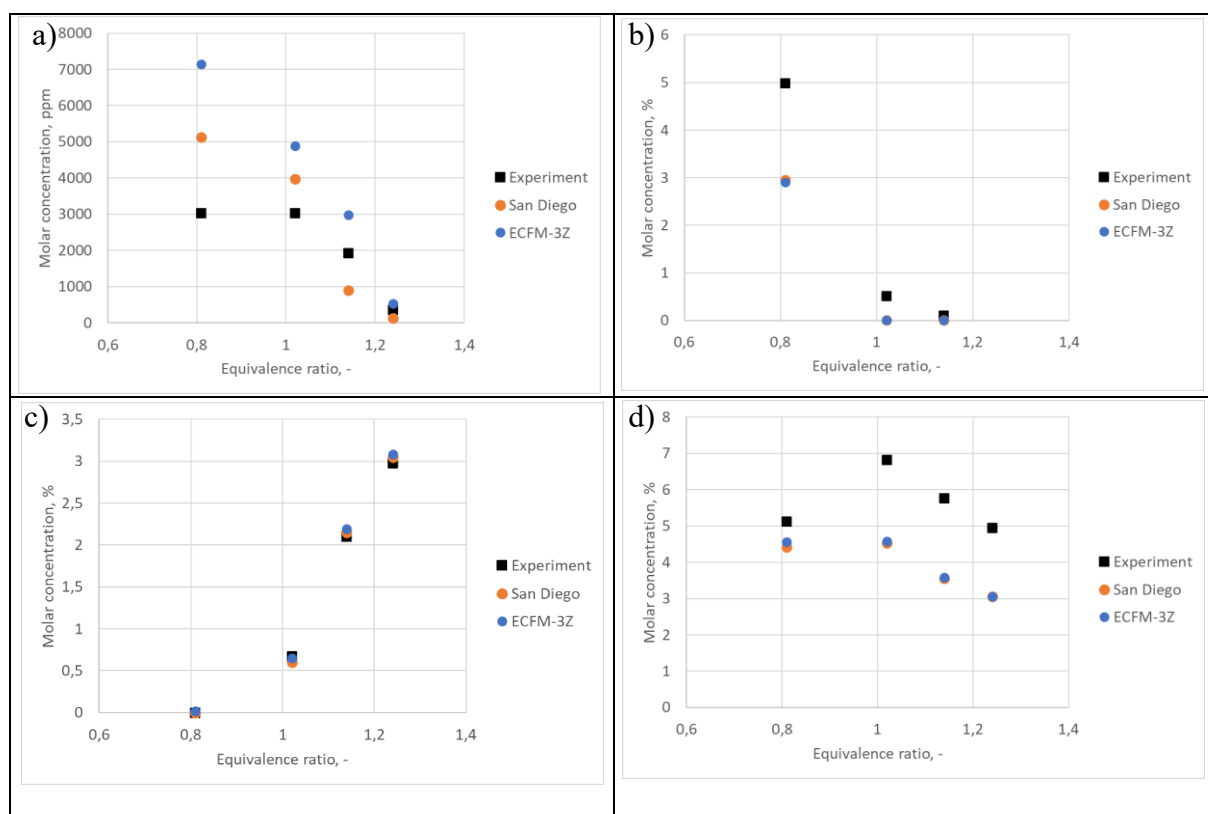
425
426
427
428

4.3. Computational Fluid Dynamics results

430 In this section, the results obtained with ECFM-3Z in the combination with pre-generated
431 dual fuel NH₃/CH₄ databases are validated against experimental data.

432 In Figure 10 a) results of NO concentration on the burner exit are compared between
433 simulation using detailed chemical model (titled “San Diego”), ECFM-3Z in the combination
434 with pre-generated dual fuel NH₃/CH₄ databases (titled “ECFM-3Z”) and experimental
435 measurements detailed in reference [22]. It can be observed that significant disparities with
436 measured data are pronounced in the lean regime, gradually decreasing as the equivalence ratio
437 is increased. It is interesting to note that detailed chemical model first overpredicts NO
438 concentration, but later overpredicts it, while ECFM-3Z consistently overpredicts experimental
439 results in the whole range of operating conditions. Across the entire equivalence-ratio sweep
440 the ECFM-3Z framework over-predicts the measured thermal-NO. This systematic bias is

441 consistent with the omission of the $\text{NNH} + \text{O}$, N_2O , and NCN prompt-NO channels in the
 442 look-up chemistry; recent studies [27] show that including these paths typically halves the error.
 443 An extended-NO table featuring the full $\text{NNH}/\text{N}_2\text{O}/\text{NCN}$ subset will be implemented in future
 444 work. In the following Figure 10 b), greater consumption of oxygen in both simulations
 445 indicates production of excess pollutants which were not observed in the experiment. Also,
 446 there is no discrepancy between detailed chemical model and tabulated approach, whilst error
 447 tend to decrease with increase in the equivalence ratio. Regarding CO concentrations (Figure
 448 10 c)), only the initial two points were reliably measured in the experiment due to the instrument
 449 surpassing its threshold at a maximum concentration of 900 ppm. Again, there is no significant
 450 difference between detailed and tabulated model. In Figure 10 d), CO_2 is underpredicted,
 451 suggesting a greater consumption of oxygen in reactions. It seems there is the need for a more
 452 comprehensive description of carbon chemistry and its interaction with nitrogen chemistry in
 453 the San Diego model. The current models seem to excessively consume oxygen in reactions
 454 that generate CO, whereas nitrogen chemistry appears to be reasonably well described. The San
 455 Diego mechanism, due to its inclusion of nitrogen chemistry in hydrocarbon combustion,
 456 demands a lot of computational time, which was significantly reduced by the tabulated
 457 approach, while the perseverance of detailed chemical mechanism's information can be
 458 considered satisfactory.
 459



460
 461 Figure 10 ECFM-3Z results in comparison with San Diego mechanism and experimental
 462 data: a) NO concentrations, b) O₂ concentrations, c) CO concentrations, d) CO₂ concentrations
 463
 464
 465

466 **5. CONCLUSION**

467 To achieve significant reductions in carbon dioxide emissions, the adoption of carbon-
468 neutral alternative fuels is mandatory. Ammonia, a promising candidate, can be blended with
469 natural gas and introduced into existing combustion systems, thereby reducing the reliance on
470 fossil fuels and the associated CO₂ emissions. This study focuses on ammonia/methane co-
471 firing in natural gas burners, employing advanced computational techniques to model and
472 optimize the combustion processes. It delivers a high-density NH₃/CH₄ chemistry database,
473 validated against four data sets and integrated into an industrial CFD solver with a significant
474 CPU saving. The San Diego mechanism was the basis for generation of laminar flame speed
475 and autoignition timing databases, covering various pressures, equivalence ratios, temperatures,
476 and reactant ratios. These databases were incorporated into the CFD code AVL Fire™ to
477 simulate combustion with the ECFM-3Z model. Validation against experimental data
478 demonstrated that the model performs well overall, with discrepancies noted in fuel-rich regions
479 and higher temperatures, attributed to limitations in the accuracy of ammonia-specific chemical
480 reactions within the San Diego mechanism. The tabulated approach significantly reduced
481 computational demand while maintaining satisfactory accuracy in representing combustion
482 dynamics, including flame stability and pollutant formation. Although NO formation was in the
483 slightly larger disagreement with both detailed mechanism and experiment, consistent trend
484 was observed in lowering discrepancies with increasing equivalence ratio. However, the study
485 also highlights areas for improvement, particularly in modelling carbon chemistry and its
486 interaction with nitrogen chemistry, to address underpredictions of CO₂ and overpredictions of
487 CO. By leveraging validated chemical mechanisms and efficient CFD workflows, the study
488 provides a robust framework for optimizing ammonia utilization in retrofitted and new
489 combustion systems. Future research should focus on refining chemical models and extending
490 the approach to other renewable fuel blends, ensuring comprehensive solutions for sustainable
491 energy transitions.

492 **ACKNOWLEDGMENT**

493 This work was funded under the auspice of the European Regional Development Fund,
494 Operational Programme Competitiveness and Cohesion 2014–2020, KK.01.1.1.04.0070. This
495 study was written also in connection with the project REFRESH – Research Excellence For
496 Region Sustainability and High-tech Industries (Reg. No. CZ.10.03.01/00/22_003/0000048),
497 financed by EU structural funds.

498 The Authors would wish to thank LOGEsoft™ for providing the software license through
499 Academic Partner Program and for their support. The authors also wish to thank the CFD
500 Development group at AVL-AST, Graz, Austria, for their continuous support and useful
501 technical discussions during the model development.

502 **REFERENCES**

- 504 [1] Valera-Medina A, Xiao H, Owen-Jones M, David WIF, Bowen PJ. Ammonia for power.
505 Progress in Energy and Combustion Science 2018;69:63–102.
506 <https://doi.org/10.1016/j.pecs.2018.07.001>.
507 [2] Mikulčić H, Baleta J, Wang X, Wang J, Qi F, Wang F. Numerical simulation of
508 ammonia/methane/air combustion using reduced chemical kinetics models. International

- 509 Journal of Hydrogen Energy 2021;46:23548–63.
510 <https://doi.org/10.1016/j.ijhydene.2021.01.109>.
- 511 [3] Arunthanayothin S, Stagni A, Song Y, Herbinet O, Faravelli T, Battin-Leclerc F.
512 Ammonia–methane interaction in jet-stirred and flow reactors: An experimental and
513 kinetic modeling study. *Proceedings of the Combustion Institute* 2021;38:345–53.
514 <https://doi.org/10.1016/j.proci.2020.07.061>.
- 515 [4] Miller JA, Smooke MD, Green RM, Kee RJ. Kinetic Modeling of the Oxidation of
516 Ammonia in Flames. *Combustion Science and Technology* 1983;34:149–76.
517 <https://doi.org/10.1080/00102208308923691>.
- 518 [5] Skreiberg Ø, Kilpinen P, Glarborg P. Ammonia chemistry below 1400 K under fuel-rich
519 conditions in a flow reactor. *Combustion and Flame* 2004;136:501–18.
520 <https://doi.org/10.1016/j.combustflame.2003.12.008>.
- 521 [6] Dagaut P, Glarborg P, Alzueta MU. The oxidation of hydrogen cyanide and related
522 chemistry. *Progress in Energy and Combustion Science* 2008;34:1–46.
523 <https://doi.org/10.1016/j.pecs.2007.02.004>.
- 524 [7] Mével R, Javoy S, Lafosse F, Chaumeix N, Dupré G, Paillard C-E. Hydrogen–nitrous
525 oxide delay times: Shock tube experimental study and kinetic modelling. *Proceedings of*
526 *the Combustion Institute* 2009;32:359–66. <https://doi.org/10.1016/j.proci.2008.06.171>.
- 527 [8] Coda Zabetta E, Hupa M. A detailed kinetic mechanism including methanol and
528 nitrogen pollutants relevant to the gas-phase combustion and pyrolysis of biomass-
529 derived fuels. *Combustion and Flame* 2008;152:14–27.
530 <https://doi.org/10.1016/j.combustflame.2007.06.022>.
- 531 [9] Klippenstein SJ, Harding LB, Glarborg P, Miller JA. The role of NNH in NO formation
532 and control. *Combustion and Flame* 2011;158:774–89.
533 <https://doi.org/10.1016/j.combustflame.2010.12.013>.
- 534 [10] Tian Z, Li Y, Zhang L, Glarborg P, Qi F. An experimental and kinetic modeling study of
535 premixed NH₃/CH₄/O₂/Ar flames at low pressure. *Combustion and Flame*
536 2009;156:1413–26. <https://doi.org/10.1016/j.combustflame.2009.03.005>.
- 537 [11] Mendiara T, Glarborg P. Ammonia chemistry in oxy-fuel combustion of methane.
538 *Combustion and Flame* 2009;156:1937–49.
539 <https://doi.org/10.1016/j.combustflame.2009.07.006>.
- 540 [12] Liu L, Wu Y, Wang Y. Numerical investigation on the combustion and emission
541 characteristics of ammonia in a low-speed two-stroke marine engine. *Fuel*
542 2022;314:122727. <https://doi.org/10.1016/j.fuel.2021.122727>.
- 543 [13] Jójka J, Kapela N, Jankowski R, Ślefarski R. Analysis of the effect of swirl flame
544 shaping on emissions from the co-firing of ammonia and methane. *Energy*
545 2024;313:133738. <https://doi.org/10.1016/j.energy.2024.133738>.
- 546 [14] Wei X, Zhang M, Wang J, Huang Z. Investigation on lean blow-off characteristics and
547 stabilization mechanism of premixed hydrogen enhanced ammonia/air swirl flames in a
548 gas turbine combustor. *Combustion and Flame* 2023;249:112600.
549 <https://doi.org/10.1016/j.combustflame.2022.112600>.
- 550 [15] Zhang J, Sui C, Zhang B, Li J. Effects of swirl intensity on flame stability and NO
551 emission in swirl-stabilized ammonia/methane combustion. *Applications in Energy and*
552 *Combustion Science* 2023;14:100138. <https://doi.org/10.1016/j.jaecs.2023.100138>.
- 553 [16] Guiberti TF, Pezzella G, Hayakawa A, Sarathy SM. Mini Review of Ammonia for
554 Power and Propulsion: Advances and Perspectives. *Energy Fuels* 2023;37:14538–55.
555 <https://doi.org/10.1021/acs.energyfuels.3c01897>.
- 556 [17] Okafor EC, Somarathne KDKA, Ratthan R, Hayakawa A, Kudo T, Kurata O, et al.
557 Control of NO_x and other emissions in micro gas turbine combustors fuelled with

558 mixtures of methane and ammonia. *Combustion and Flame* 2020;211:406–16.
559 <https://doi.org/10.1016/j.combustflame.2019.10.012>.

560 [18] Jiang Y, Gruber A, Seshadri K, Williams F. An updated short chemical-kinetic nitrogen
561 mechanism for carbon-free combustion applications. *Int J Energy Res* 2020;44:795–810.
562 <https://doi.org/10.1002/er.4891>.

563 [19] Ban M, Duic N. Adaptation of n-heptane autoignition tabulation for complex chemistry
564 mechanisms. *Therm Sci* 2011;15:135–44. <https://doi.org/10.2298/TSCI100514077B>.

565 [20] Jurić F, Ban M, Priesching P, Schmalhorst C, Duić N, Vujanović M. Numerical
566 modeling of laminar flame speed and autoignition delay using general fuel-independent
567 function. *Fuel* 2022;323:124432. <https://doi.org/10.1016/j.fuel.2022.124432>.

568 [21] Colin O, Benkenida A. The 3-Zones Extended Coherent Flame Model (Ecfm3z) for
569 Computing Premixed/Diffusion Combustion. *Oil & Gas Science and Technology - Rev*
570 *IFP* 2004;59:593–609. <https://doi.org/10.2516/ogst:2004043>.

571 [22] Valera-Medina A, Marsh R, Runyon J, Pugh D, Beasley P, Hughes T, et al. Ammonia–
572 methane combustion in tangential swirl burners for gas turbine power generation.
573 *Applied Energy* 2017;185:1362–71. <https://doi.org/10.1016/j.apenergy.2016.02.073>.

574 [23] Xiao H, Lai S, Valera-Medina A, Li J, Liu J, Fu H. Experimental and modeling study on
575 ignition delay of ammonia/methane fuels. *Int J Energy Res* 2020;44:6939–49.
576 <https://doi.org/10.1002/er.5460>.

577 [24] Han X, Wang Z, Costa M, Sun Z, He Y, Cen K. Experimental and kinetic modeling
578 study of laminar burning velocities of NH₃/air, NH₃/H₂/air, NH₃/CO/air and
579 NH₃/CH₄/air premixed flames. *Combustion and Flame* 2019;206:214–26.
580 <https://doi.org/10.1016/j.combustflame.2019.05.003>.

581 [25] Okafor EC, Naito Y, Colson S, Ichikawa A, Kudo T, Hayakawa A, et al. Experimental
582 and numerical study of the laminar burning velocity of CH₄–NH₃–air premixed flames.
583 *Combustion and Flame* 2018;187:185–98.
584 <https://doi.org/10.1016/j.combustflame.2017.09.002>.

585 [26] Rocha RC, Zhong S, Xu L, Bai X-S, Costa M, Cai X, et al. Structure and Laminar Flame
586 Speed of an Ammonia/Methane/Air Premixed Flame under Varying Pressure and
587 Equivalence Ratio. *Energy Fuels* 2021;35:7179–92.
588 <https://doi.org/10.1021/acs.energyfuels.0c03520>.

589 [27] A A, S M, H S, M A, P W, D P, et al. Evolution of ammonia reaction mechanisms and
590 modeling parameters: A review. *Applications in Energy and Combustion Science*
591 2023;15:100175. <https://doi.org/10.1016/j.jaecs.2023.100175>.

592
593
594